Radiation magnetohydrodynamic simulation of plasma formed on a surface by a megagauss field

A. A. Esaulov, B. S. Bauer, V. Makhin, R. E. Siemon, I. R. Lindemuth, and T. J. Awe
Department of Physics, University of Nevada, Reno, Nevada 89557, USA

R. E. Reinovsky
Los Alamos National Laboratory, Los Alamos, New Mexico 87545, USA

K. W. Struve, M. P. Desjarlais, and T. A. Mehlhorn
Sandia National Laboratories, Albuquerque, New Mexico 87185, USA

(Received 4 October 2007; revised manuscript received 6 January 2008; published 11 March 2008)

Radiation magnetohydrodynamic modeling is used to study the plasma formed on the surface of a cylindrical metallic load, driven by megagauss magnetic field at the 1 MA Zebra generator (University of Nevada, Reno). An ionized aluminum plasma is used to represent the "core-corona" behavior in which a heterogeneous *Z*-pinch consists of a hot low-density corona surrounding a dense low-temperature core. The radiation dynamics model included simultaneously a self-consistent treatment of both the opaque and transparent plasma regions in a corona. For the parameters of this experiment, the boundary of the opaque plasma region emits the major radiation power with Planckian black-body spectrum in the extreme ultraviolet corresponding to an equilibrium temperature of 16 eV. The radiation heat transport significantly exceeds the electron and ion kinetic heat transport in the outer layers of the opaque plasma. Electromagnetic field energy is partly radiated (13%) and partly deposited into inner corona and core regions (87%). Surface temperature estimates are sensitive to the radiation effects, but the surface motion in response to pressure and magnetic forces is not. The general results of the present investigation are applicable to the liner compression experiments at multi-MA long-pulse current accelerators such as Atlas and Shiva Star. Also the radiation magnetohydrodynamic model discussed in the paper may be useful for understanding key effects of wire array implosion dynamics.

DOI: 10.1103/PhysRevE.77.036404 PACS number(s): 52.58.Lq, 52.65.Kj, 52.25.Os

I. INTRODUCTION

Different approaches to plasma fusion research can roughly be categorized as either magnetic confinement fusion energy (MFE) [1] or inertial confinement fusion (ICF) [2]. The concept of the magnetized target fusion (MTF) [3] is in the area that is intermediate between MFE and ICF in time and density scales. A number of plasma configurations and plasma compression schemes, which include the compression of target plasma by a solid liner, have been proposed for MTF. Liner methods can be further classified by the type and configuration of target plasma. Cylindrical liners are used to compress field-reversed configuration (FRC) [4–7] as a target plasma. Alternatively, the inverse pinch configuration (hardcore *Z* pinch) [8–10] has been proposed as a target plasma to be compressed by a cylindrical liner. More complex, hybrid cylindrical and spherical liner configurations are utilized in the MAGO (brief for the ''magnetic compression'' in Russian) concept [11–13].

In addition to the MTF-related experiments the electromagnetically driven implosions of metallic liners have some other important applications, such as magnetic flux compression [14] and generation of high energy density environments in near solid density materials for studying instabilities, material properties under extreme conditions, and hydrodynamics in complex geometries [15]. Although the requirements on the conditions of the liner are different for each experiment, most applications seek a high degree of symmetry and uniformity in the liner after implosion and a well-defined, smooth, solid density inner surface (see, for example, the discussion in Ref. [15]).

During acceleration the outer surface of a liner (the interface with the magnetic field) is unstable to the growth of small perturbations due to the Rayleigh-Taylor (RT) instability mechanism. The material strength mitigates the growth of RT modes [16]. However, the ohmic heating of the liner during the implosion effectively reduces the material strength after the phase transition to a liquid. The RT instability is known to be the most destructive one for the implosion of light mass wire arrays with short pulse multi-MA current accelerators on Saturn [17] and *Z* [18] facilities at Sandia National Laboratories. Melting and destruction of the liner can be significantly delayed by imploding substantially heavier loads at long-pulse current accelerators, such as the 16-MA ($t_{\mathrm{rise}}=8\ \mu$s) Shiva Star [19] and 32-MA ($t_{\mathrm{rise}}=3.7\ \mu$s) Atlas [15] facilities or 100 MA explosive magnetic compression generator (EMG) [20]. For these particular experiments it is very important to understand the physics behind magnetic field penetration into a solid liner, including the processes at the outer liner surface, such as liner material melting, vaporization, and plasma formation.

A recent experimental campaign on the 1 MA Zebra facility at the University of Nevada, Reno aimed to recreate the processes that govern plasma formation at the liner surface on multi-MA generators, be exploding cylindrical aluminum and copper loads with diameters of 1–2 mm. Experimental diagnostics included optical imaging, streak camera, magnetic field probes, photodiodes, photomultipliers, and laser probing. Theoretical investigation by means of radiation magnetohydrodynamic (MHD) simulations can help to interpret the results of these experiments, to understand the phys-

ics behind the processes hidden from direct experimental observations, and to perform proper scaling of these results to multi-MA current accelerators.

The model of processes at the liner surface emerges from the interplay of magnetic diffusion, hydrodynamics, and kinetic and radiation energy transport. Similar conditions are realized in the early evolution of a Z pinch, formed by the MA-scale electric discharge through a solid-state object, such as a metallic wire or a frozen deuterium filament [21–23]. In this case the nonhomogeneous Z-pinch structure [24], often referred to in the literature as the "core-corona" structure, is formed. If a Z pinch is formed by the explosion of a higher-Z material, such as aluminum, we should also expect the significantly higher radiation dynamic effects in the pinch corona, which could modify the earlier results obtained in Refs. [21,24].

The next section of this paper is devoted to the discussion of corona production and expansion dynamics. The ablation time, or the time period for the core-corona coexistence, is calculated for the typical wire array and liner compression experiments. The initial and boundary conditions for the simulations are discussed. The radiation MHD simulations are performed, using the different current pulse shapes and radiation models. The third section is devoted to the discussion of the radiation model that takes into account both opaque and transparent plasmas, and how the effects associated with radiation dynamics influence the structure and parameters of the corona. A special subsection is devoted to the qualitative comparison of the simulation results with the raw experimental data. The conclusion remarks are given in the fourth section.

II. PLASMA PRODUCTION AT LOAD SURFACE

MHD simulations in the scope of the present investigation have been performed using the two-dimensional, two-temperature, resistive and radiation MHD code POS [25]. Code POS solves the system of the MHD equations on the Eulerian spatial grid [in the (r,z) plane] using the same method of numerical integration as the one described in Ref. [26]. Temperatures of the electron T_e and ion T_i plasma components are treated separately.

The kinetic transport coefficients, such as the electron and ion thermal conductivities, the electric resistance of plasma, and the rate of thermal transfer between the electrons and ions, are calculated in two-polynomial approximation [27] for arbitrary values of the mean ion charge and the electron and ion magnetization degrees. The exact expressions for these coefficients may be found in Refs. [28,29]. The approximation of local thermodynamic equilibrium (LTE) is used to calculate the ionization balance according to generalized Saha equation for multiply ionized atoms in the Zeldovich-Raizer model [30]. A similar MHD model has been exploited in the MHD code PICA, and was applied for simulations of the explosion of frozen deuterium fibers [21,24] and capillary discharges (see, for example, Refs. [28,29]).

The radiation in optically thin plasma is coupled to the energy balance in the electron component of plasma as the volume power loss [25]. Consideration of the radiation transport in optically thick plasma in the one group flux limiting radiation diffusion approximation is the new addition to the model that will be discussed in the next section of this paper.

The approach applied in this paper to the simulations of plasma production at the load surface is the same as the one applied to the simulation of the electric explosion of the metallic wires or frozen deuterium fibers [21,24]. According to this approach at the initial moment the load material is treated as a cool dense plasma, having the temperature of ~ 1 eV and solid state density. In the case of the thin metallic wire the plasma bulk quickly (on the time scale of the current pulse rise) heats up to the temperatures that are well above the phase transition levels. This feature of wire explosion dynamics validates the above approach. There are, however, some restrictions on application of such an approach to the liner compression experiments.

A. Relation between the ablation and implosion times

One of the critical parameters of the dynamics of imploding liners or wire array loads is the ratio of the ablation time $t^{(a)}$ to the implosion time $t^{(i)}$. If $t^{(a)} < t^{(i)}$, then the bulk of the liner material is vaporized and turned into plasma during the implosion. In the opposite case $t^{(a)} \gg t^{(i)}$ we should expect the significant mass of the liner material to remain at liquid, or even at solid phase. The former condition is typically fulfilled in the experiments with imploding wire array loads, where $0.5 < t_w^{(a)}/t_w^{(i)} < 1$, while the latter condition is preferable for the liner compression experiments for the reasons mentioned, for example, in Ref. [15].

The implosion time of a cylindrical load, such as a liner or a wire array, can be calculated with the so-called zero-dimensional (0D) model. The earliest discussion of this model may be found in Ref. [31]. The 0D model describes the implosion of a thin shell of radius r and mass per unit length m_L

$$\frac{d^2r}{dt^2} = -\frac{\mu_0}{4\pi}\frac{I^2}{m_L r}. \tag{1}$$

As was shown in Ref. [31], in the case of the constant current pulse I=const the above equation can be solved analytically, and the implosion time is defined by the following equation:

$$t^{(i)} = r_0\sqrt{\frac{2\pi^2}{\mu_0}\frac{m_L}{I^2}}, \tag{2}$$

where r_0 is the initial load radius.

The ablation rate of the wire in array is believed to be proportional to the square of electric current (see, for example, discussion in Ref. [32]). Then, the ablation time should be inversely proportional to the ablation rate and directly proportional to the ablated mass per unit length $t^{(a)} \propto m_L/I^2$. On the other hand, from Eq. (2) it follows that $m_L/I^2 \propto [t^{(i)}]^2$. Hence, if the implosion time is matched with the current rise time $t^{(i)} \approx t_{\text{rise}}$, then $t^{(a)}/t^{(i)} \propto t_{\text{rise}}$ and $m_L/I^2 \propto t_{\text{rise}}^2$.

A substantial difference in current rise time, for example, between Z and Atlas current accelerators results in signifi-

cantly different ablation regimes for the imploding loads at these pulsed power facilities. In fact the ratio of the ablation time to implosion time for the liner at the Atlas facility can be estimated as $t_l^{(a)}/t_l^{(i)} \approx 40$, instead of $t_w^{(a)}/t_w^{(i)} < 1$ for wire arrays at the Z facility. It should be also mentioned that the typical liner load mass at the Atlas facility is more than a factor of 10^3 higher than the mass of the typical wire array load at the Z facility.

Because of the very long liner ablation time $t_l^{(a)}/t_l^{(i)} \gg 1$, the major mass fraction of the liner does not go through the phase transitions to a gas or plasma during the implosion and remains at liquid, or even at solid phase. This fact imposes severe constraints on application of the conventional MHD model that is based on the equations of gas dynamics. In the general case the extension of the MHD model is required to take into account incompressible fluid dynamics or the material strength (as it was performed, for example, in Ref. [15]).

However, the behavior of plasma near the surface and its radiation properties occur at temperatures well above the levels related to the phase transitions. With the proper set of assumptions, discussed below, the dynamics of the bulk of load material and ablation process at the load surface can be described in a single MHD simulation with a descent accuracy, using the "core-corona" model of the heterogeneous Z pinches in the dissipative regime [21,24].

B. Statement of problem for MHD modeling

In order to get an adequate description of the dynamics of an initially solid rod in the core-corona approximation one has to balance the material pressure with the magnetic field pressure. The load mass and size, and consequently the material density, are predefined by the conditions of the experiment. Yet, by changing the initial temperature of the load material we can manipulate the gas (or plasma) pressure. The equilibrium between the plasma pressure and the magnetic field pressure is provided by the Bennett relation

$$I_B^2 = \frac{8\pi T}{\mu_0}\frac{m_L}{Am_A}, \tag{3}$$

where T is the temperature (here and below in this paper the temperature is expressed in energy units), A is the atomic weight of the material, and m_a is the atomic mass unit. In the above equation we assume low-temperature $T \leqslant 1$ eV and weakly ionized $\bar{Z} \ll 1$ plasma ($\bar{Z}$ is the mean ion charge).

In the experiments at the Zebra facility the aluminum cylindrical rod with the diameter $\phi = 1$ mm has been used as a load with the mass per unit length $m_L = 2.1 \times 10^{-3}$ g/mm. A typical Zebra current pulse can be described with a good accuracy by the following shape:

$$I(t) = I_{\max} \sin^2\left(\frac{\pi}{2}\frac{t}{t_{\max}}\right), \tag{4}$$

where $I_{\max} = 1$ MA and $t_{\max} = 120$ ns.

If the load material is represented by the uniform cylindrical plasma column with the room temperature $T = 0.026$ eV, then the equilibrium value of the total electric current according to Eq. (3) is $I_B = 6$ kA. Taking into account the current pulse shape, given by Eq. (4), the load material pressure and the magnetic field pressure will be approximately balanced at the beginning of the current pulse. Yet, after ≈ 20 ns and for the rest of the time the magnetic field pressure will exceed the pressure of the load material, as we should expect the significant compression of the load material by the strong inward shock, driven by the magnetic piston.

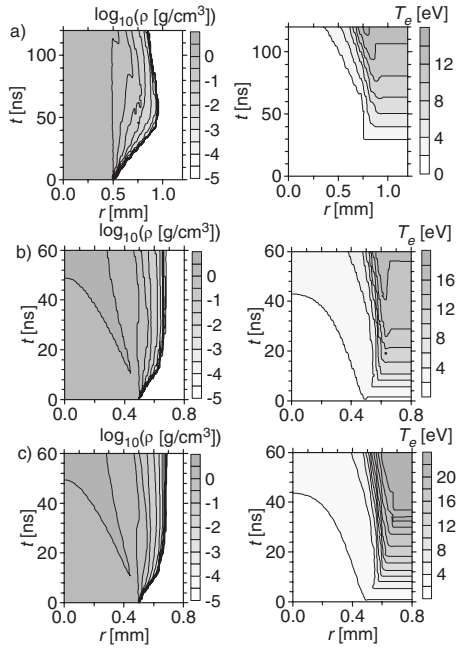

FIG. 1. Time-radius plots of the contour levels of the decimal logarithm of plasma density $\log_{10}\rho$ and the electron temperature T_e presented for three different simulations: (a) full current pulse [Eq. (4)], (b) truncated current pulse [Eq. (5), $t_{sh} = 60$ ns], and (c) truncated current pulse without radiation. Note that the plot (a) and the plots (b) and (c) are presented in different time and radial coordinate scales.

If we increase the material temperature to 1 eV, then the equilibrium current value becomes 0.39 MA. Thus, the material pressure and the magnetic field pressure will be in approximate balance in the middle of the current pulse, when we should expect the increasing rate of plasma production at the load surface. For this reason the initial temperature of load material $T = 1$ eV will be used for the MHD simulations, which will be discussed below in this paper.

C. Dynamics of corona plasma at load surface

The results of the MHD simulations performed with the different current pulse shapes and different models are presented by the time-radius contour plots in Fig. 1. Correspondent radial profiles at the current pulse maximum are shown in Fig. 2.

The simulation with the full current pulse, described by Eq. (4), in Fig. 1(a) represents the actual current pulse shape. Yet, this simulation overestimates the plasma production rate at the load surface. Because of the initial imbalance between

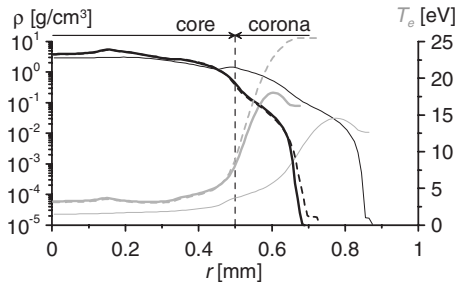

FIG. 2. Radial profiles of plasma mass density ρ (black lines) and the electron temperature T_e (gray lines) at current pulse maximum given for three different simulations, corresponding to the ones shown in Fig. 1: full current pulse (fine lines), truncated current pulse (solid lines), and truncated current pulse without radiation (dotted lines). Initial radius of the load is represented by the vertical dotted line, which can also be considered as the nominal boundary between the core and corona plasma in simulations with truncated current pulse.

the plasma pressure and the magnetic field pressure the plasma that represents the bulk of the load material is allowed to expand almost freely until it can be confined by the increasing magnetic field pressure at $t \approx 60$ ns.

However, the production of plasma at the load surface should be governed by the different mechanism, which is the ohmic heating of the thin layer of the load material, adjacent to the load surface. The initial width of this layer is defined by the skin depth of the metal. The ohmic heating leads to the melting, vaporization, and ionization of the load material, while the increasing pressure of the ablated material becomes high enough to counteract the magnetic field pressure.

Plasma, created by almost free expansion of the load material in simulation with the full current pulse, is relatively cold and thus cannot build the additional pressure required to counteract the magnetic field pressure to continue the expansion. In Fig. 1(a) we can observe the retraction of the boundary between the magnetic field and plasma after its initial expansion.

This flaw, however, can be significantly reduced in the MHD simulations with the truncated current pulse shape

$$I(t) = I_{\max} \sin^2\left(\frac{\pi}{2}\frac{t + t_{\rm sh}}{t_{\max}}\right). \tag{5}$$

The new parameter $t_{\rm sh}$ in the above equation represents the time shift between the start of the MHD simulation and the beginning of the current pulse.

Figure 1(b) shows the simulation results using the truncated current pulse $t_{\rm sh}=60$ ns. The simulation starts when the value of total current through plasma is already equal to 0.5 MA, which is half of its maximum amplitude. In this case from the very beginning the magnetic field pressure effectively inhibits the "hydrodynamic" corona plasma production due to the free expansion of load material. At the same time the initially discontinuous magnetic field profile at the plasma edge significantly enhances the surface heating. The latter mechanism of the corona plasma production through the ohmic heating of the load material seems to be the most adequate one for the set of assumptions used in this paper.

As we can see from Fig. 1(b), the rapid expansion of the corona plasma stops after $\approx$20 ns of the simulation. For the rest of the current pulse until its maximum the corona plasma remains in almost perfect equilibrium with the magnetic field. An obvious explanation of this effect would be a compensation of the increasing magnetic field pressure as the current rises by the plasma pressure increase due to the Ohmic heating of the corona.

Generally speaking, the radial profiles of mass density and electron temperature in Fig. 2 resemble the ones obtained in simulations of the electrical explosion of frozen deuterium filaments [21,24]: one can clearly separate a cold dense core and a hot low density corona. However, the corona fraction of the low-Z deuterium plasma extends to a distance of the several core radii. Contrary to that, in the case of the higher-Z aluminum plasma the extension of the corona fraction is much smaller, and is only a fraction of the core radius. Although the transition from core to corona fractions of plasma is smooth, one can nominally place the boundary between these plasma regions, for example, judging the plasma temperature profile. For the simulations with truncated current pulse in Fig. 2 the nominal boundary between core and corona can be placed at the initial position of the load surface.

Another distinct feature of the aluminum pinch compared to the deuterium one is the shape of the density profiles, shown in Fig. 2. These profiles are extremely steep near the outer edge of the corona. The density drops three orders of its magnitude in a distance of a few tens of microns. This feature is likely to be predefined by the increased heat capacitance of the higher-Z plasma due to much higher ionization energy. The MHD simulation that disregards the radiation power losses is presented in Fig. 1(c). Comparing the data in Figs. 1(b), 1(c), and 2 we can conclude that the radiation effects make only a small contribution to the steepness of the density profile.

III. RADIATION FEATURES OF THE ABLATED PLASMA

Because the corona has higher temperature, it is the corona plasma that should be responsible for the major radiation effects. The radiation MHD model in the code POS treats only the electron and ion temperatures of plasma, without special consideration of the radiation temperature. The radiation effects that can be taken into account by this model are the radiative cooling of plasma and the enhanced heat transport in plasma. The intensity of both these processes depends on the ratio of the mean free path l_ν of the photon of energy $h\nu$ in plasma to the typical spatial scale of plasma inhomogeneities (for example, the radial size of the computational domain a). If it is not specifically pointed out otherwise, all discussions and figures below in this section will be referred to the simulation with the truncated current pulse.

A. Opaque and transparent plasma regions

The radiation transfer equation for the specific intensity of the frequency dependent nonequilibrium radiation $I_{\nu n}$ in the

direction **n** can be written as [30] (see also Refs. [33,34])

$$\frac{1}{c}\frac{\partial I_{\nu n}}{\partial t} + \mathbf{n}\cdot\nabla I_{\nu n} = \frac{I_\nu - I_{\nu n}}{l_\nu}, \tag{6}$$

where I_ν is the specific intensity of the equilibrium black-body radiation

$$I_\nu = \frac{2h}{c^2}\frac{\nu^3}{e^{h\nu/T}-1}. \tag{7}$$

Similarly to Eq. (6) one can write the conservation law for the frequency-dependent radiation energy density $\varepsilon_{\nu n}$

$$\frac{1}{c}\frac{\partial \varepsilon_{\nu n}}{\partial t} + \mathbf{n}\cdot\nabla\varepsilon_{\nu n} = \frac{\varepsilon_\nu - \varepsilon_{\nu n}}{l_\nu} \tag{8}$$

by integrating over the all solid angle Ω

$$\varepsilon_{\nu n} = \frac{1}{c}\int_0^{4\pi} I_{\nu n}(\Omega)d\Omega. \tag{9}$$

In Eq. (8) $\varepsilon_\nu = 4\pi I_\nu / c$ is the specific energy of the isotropic black-body radiation.

Neglecting the time derivative term in the left-hand side of Eq. (6), one can roughly estimate the specific intensity of nonequilibrium radiation as

$$I_{\nu n} \approx \frac{I_\nu}{1 + l_\nu / a}. \tag{10}$$

Then, two extreme cases of the opaque $(l_\nu/a) \ll 1$ and transparent $(l_\nu/a) \gg 1$ plasmas can be considered.

As it was shown in Refs. [33,34], the classic diffusion theory result can be derived from Eq. (6), arguing that the problem is collision dominated if the radiation intensity $I_{\nu n}(\Omega)$ is isotropic, and hence the time derivative in the left-hand side of Eq. (6) can be ignored. Thus, we get the well known classical Fick's law of diffusion

$$\mathbf{F}_{\nu n} = -\frac{c l_\nu}{3}\nabla \varepsilon_{\nu n}, \tag{11}$$

where $\mathbf{F}_{\nu n}$ is the radiation flux

$$\mathbf{F}_{\nu n} = \int_0^{4\pi} I_{\nu n}\mathbf{\Omega} d\Omega. \tag{12}$$

In opaque plasma, according to the estimation (10), the specific intensity of the nonequilibrium radiation is almost equal to the specific intensity of the equilibrium black-body radiation $I_{\nu n} \approx I_\nu$. Small deviation from the equilibrium will be treated in a gray (one group) diffusion approximation by the integration over the whole frequency range.

In one group approximation the expression for the radiation energy density ε_{rad} in opaque plasma becomes

$$\varepsilon_{\text{rad}} = \int_0^\infty \varepsilon_{\nu n} d\nu \approx \frac{8\pi h}{c^3}\int_0^\infty \frac{\nu^3 d\nu}{e^{h\nu/T}-1} = \frac{4\sigma T_e^4}{c}, \tag{13}$$

where σ is the Stefan-Boltzmann constant

$$\sigma = \frac{2\pi^5}{15c^2h^3}. \tag{14}$$

Equation (11) for the radiation flux in one group diffusion approximation will be

$$\mathbf{F}_{\text{rad}} = \int_0^\infty \mathbf{F}_{\nu n} d\nu = -\frac{16}{3}\sigma T_e^3 \bar{l}_R \nabla T_e, \tag{15}$$

where $\bar{l}_R$ is the Rosseland mean free path of photons

$$\bar{l}_R = \frac{15}{4\pi^4}\int_0^\infty l_\nu \frac{u^4 e^u du}{(e^u - 1)^2}. \tag{16}$$

In the above equation $u = h\nu/T$ is the dimensionless parameter of integration.

Fick's radiation diffusion law (11) does not limit the value of the radiation flux $\mathbf{F}_{\text{rad}}$. Meanwhile, the radiation flux cannot exceed its upper bound limit, defined by the specific intensity I_ν of the equilibrium black-body radiation. Since we consider only the radial gradients of all values

$$|F_{\text{rad}}| = |\mathbf{e}_r \cdot \mathbf{F}_{\text{rad}}| \leqslant \int_0^\infty \int_\Omega I_\nu |\mathbf{e}_r \cdot \mathbf{\Omega}| d\Omega d\nu = \sigma T_e^4, \tag{17}$$

where $\mathbf{e}_r$ is the unit vector in the radial direction. The above equation represents the flux limiting feature of the radiation diffusion approximation [33,34], which in the general case is expressed as $|\mathbf{F}_{\nu n}| \leqslant \varepsilon_{\nu n} c$ in terms of Eq. (11).

Equations (15) and (17) provide the applicability condition for the diffusion approximation, imposing the restriction on the gradient of electron temperature

$$|\nabla T_e| \leqslant \frac{3}{16}\frac{T_e}{\bar{l}_R}. \tag{18}$$

If condition (18) is not fulfilled, then the flux limiter approach dictates the replacement of the Rosseland mean free path $\bar{l}_R$ with its effective value $\bar{l}_R^*$

$$\bar{l}_R^* = \min\left[\bar{l}_R, \frac{3}{16}\frac{T_e}{\nabla T_e}\right]. \tag{19}$$

In transparent plasma the specific intensity of nonequilibrium radiation is much less than the specific intensity of the equilibrium black-body radiation $I_{\nu n} \approx (a/l_\nu) I_\nu \ll I_\nu$. Large mean free path of the photons $l_\nu \gg a$ means that being emitted the photons just escape the plasma with no interaction with electrons or ions. The conservation law for the radiation energy density $\varepsilon_{\nu n}$ can be derived from Eq. (8):

$$\frac{1}{c}\frac{d\varepsilon_{\nu n}}{dt} = \frac{1}{c}\frac{\partial \varepsilon_{\nu n}}{\partial t} + \mathbf{n}\cdot\nabla\varepsilon_{\nu n} = \int_0^{4\pi}\frac{I_\nu - I_{\nu n}}{c l_\nu} d\Omega. \tag{20}$$

Neglecting the term $I_{\nu n}$ in the numerator of the subintegral expression in the above equation and applying the one group approximation we get the expression for the local radiative cooling rate Q_{rad}

$$Q_{\rm rad} = \frac{d}{dt}\int_0^\infty \varepsilon_{\nu m} d\nu = 4\pi \int_0^\infty \frac{I_\nu}{l_\nu} d\nu = 4\frac{\sigma T_e^4}{l_R}, \qquad (21)$$

where the mean free path l_R is now defined as

$$\frac{1}{l_R} = \frac{15}{\pi^4}\int_0^\infty \frac{1}{l_\nu}\frac{u^3 du}{e^u - 1}. \qquad (22)$$

As we can see from the above discussion, the description of the opaque ($\bar{l}_R \ll a$) and transparent ($l_R \gg a$) plasma regions in one group approximation exploits two definitions of the optical depth of plasma. However, both parameters $\bar{l}_R$ and l_R represent the average values of the mean free path of photons l_ν, integrated with the different weight functions [see Eqs. (16) and (22)]. In the major parameter range the values $\bar{l}_R$ and l_R differ only by a factor of ~ 3.

The photon mean free path l_ν has been calculated using the Kramers-Unzöld formula [30] that takes into account free-free and free-bound electron transitions. Then, the expression for the optical depth of plasma becomes (see also Ref. [25])

$$\frac{1}{l_R} = \frac{15}{4\sqrt{3}}\frac{e^6}{\pi^5 \varepsilon_0^3 hc}\frac{1}{T_e^3}\sum_{m=1}^{Z} m^2 N_m \chi_m e^{-\chi_m/T_e}, \qquad (23)$$

where Z is the atomic nucleus charge, N_m is the number of ions with charge m per unit volume, and χ_m is the mth ionization potential. Radial profile $l_R(r)$ is shown in Fig. 3(a).

Because of the steepness of the density profile at the outer corona region, the radial profile of l_R is also steep. The value of l_R changes five orders of its magnitude in a thin layer of the width 40 μm. Within this layer the value $l_R = a$ should be reached inside the spatial grid cell with the coordinate r_s. The steepness of the function $l_R(r)$ ensures the fulfillment of the condition $\bar{l}_R \ll a$ for all cells with coordinates $r_i < r_s$ and the condition $l_R \gg a$ for all cells with coordinates $r_i > r_s$ at reasonable spatial grid resolution (in the discussed simulations $\Delta r = 7$ μm).

Thus, we can treat the radiation properties in the region $r < r_s$ as in opaque plasma and in the region $r > r_s$ as in transparent plasma. Special consideration will be given for a single computational cell with coordinate r_s, which is a solution of the implicit equation $l_R(r_s) = a$.

In the two-temperature approximation the radiation effects are assumed to affect the local energy balance of the electron component of plasma and are accounted for by the additional terms in the evolution equation for the specific internal energy of the electrons ε_e

$$\frac{d\varepsilon_e}{dt} = \cdots - \nabla \cdot [\mathbf{F}_e + \mathbf{F}_{\rm rad}] - Q_{\rm rad}$$

$$= \cdots + \nabla \cdot [(\kappa_e + \kappa_{\rm rad}) \nabla T_e] - Q_{\rm rad}, \qquad (24)$$

where $\mathbf{F}_e$ is the electron thermal flux, κ_e is the electron thermal conductivity coefficient (exact expression can be found in Refs. [28,29]), and $\kappa_{\rm rad}$ is the effective radiation diffusion coefficient

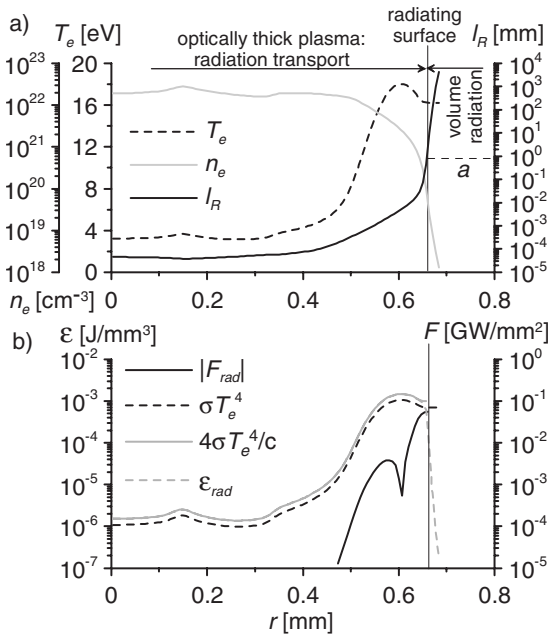

FIG. 3. (a) Radial profiles of the electron density n_e, the electron temperature T_e, and the optical depth of plasma l_R at the maximum current ($t = 60$ ns). Fine dotted horizontal line represents the position of the space scale a in the ordinate axis. (b) Absolute value of the radiation flux $|F_{\rm rad}|$ and its limiter σT_e^4 [Eq. (17)], equilibrium black-body radiation energy density $4\sigma T_e^4/c$, and the radiation energy density $\varepsilon_{\rm rad}$ according to Eq. (26). On both plots (a) and (b) the fine vertical lines denote the position of the radiating surface $r = r_s$, which separates optically thick ($\bar{l}_R \ll a$) and optically thin ($l_R \gg a$) plasma regions.

$$\kappa_{\rm rad} = \frac{16}{3}\sigma T_e^3 \bar{l}_R^*. \qquad (25)$$

It is assumed that in the opaque plasma region $r < r_s$ we should take $Q_{\rm rad}(r) \equiv 0$, while in the transparent plasma region $r > r_s$ we should take $\kappa_{\rm rad} \equiv 0$.

In order to describe the radiation features at the layer $r = r_s$ within the two-temperature approximation, we have to use the terms of both opaque and transparent plasma descriptions. Using the estimation (10) and the one group approximation the expression for the radiation energy density (13) can be extended for the whole plasma region

$$\varepsilon_{\rm rad}(r) = \frac{4\sigma T_e^4(r)}{c}\frac{1}{1 + l_R(r)/a}. \qquad (26)$$

As we can see from the data in Fig. 3(b), the condition (18) is fulfilled throughout the whole opaque plasma region $r < r_s$. However, at $r = r_s$ there is a strong negative gradient of the radiation energy density $\nabla \varepsilon_{\rm rad}(r)$ that suggest the outward radiation flux, defined by the flux limiting condition (17)

$$F_{\rm rad}(r_s) = \sigma T_e^4(r_s). \qquad (27)$$

The radiation flux (27) cannot be reabsorbed by the layer of transparent plasma at $r_s < r \leq a$. The radiation power loss

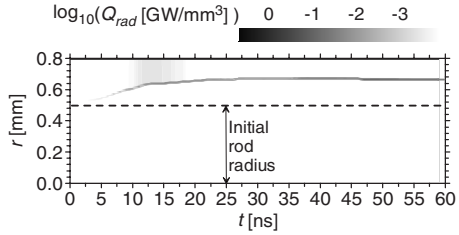

FIG. 4. Contour levels of the decimal logarithm of radiation power per unit volume $Q_{\rm rad}$ as a function of pinch radius r and time t. The initial position of the rod surface is shown by the horizontal dotted line.

at the layer $r=r_s$ can be accounted for by the volume radiation cooling term $Q_{\rm rad}(r_s)$, if we renormalize the radiation flux from the surface $\Delta S(r_s)$ of the computational cell to a power loss in the volume $\Delta S(r_s)\Delta r$ of this cell

$$Q_{\rm rad}(r_s) = \frac{\Delta S(r_s)\cdot F_{\rm rad}}{\Delta S(r_s)\Delta r} = \frac{\sigma T_e^4(r_s)}{\Delta r}. \tag{28}$$

Although the above expression for $Q_{\rm rad}(r_s)$ contains the spatial grid step Δr in the radial direction, the grid resolution does not affect the value of the total power per unit load length $2\pi r_s \sigma T_e^4(r_s)$, emitted by the radiating surface at $r=r_s$.

The evolution of the radial profile of the volume radiative cooling term in time is shown in Fig. 4 by the contour plot $Q_{\rm rad}(r,t)$. During the whole simulation the volume radiation power is defined predominantly by the emission from the layer $r=r_s$ [Eq. (28)]. Hence, the contour lines in Fig. 4 mostly reproduce the expansion dynamics of the radiating surface $r_s(t)$, which is consistent with the mass density evolution plot in Fig. 1(b).

B. Radiation dynamics of the corona plasma

According to simulation results, after the first 20 ns the corona plasma comes to a quasiequilibrium with the magnetic field. In this situation the influence of the advection terms on the energy balance of the electron plasma component is negligible. In addition to the terms, listed in Eq. (24), the important role in the electron energy balance is played by the ohmic heating.

Figure 5 presents radial profiles of the coefficients of electron κ_e and ion κ_i thermal conductivities, and the radiation diffusion coefficient $\kappa_{\rm rad}$. Because of the strong dependence on electron temperature and direct proportionality to the Rosseland mean free path $\kappa_{\rm rad} \propto T_e^3 l_R^*$ the radiation diffusion coefficient dramatically increases toward the outer boundary of the opaque plasma region at $r=r_s$. At the same time the high magnetization degree of the electrons in low-density corona plasma effectively dampens the electron heat transport. Because of these reverse tendencies the radiation transport dominates the kinetic heat transport $\kappa_{\rm rad} \gg \kappa_e, \kappa_i$ in the outer corona region until the boundary of the opaque plasma.

The measurements, performed in experiments with exploding metallic wires [35], show that the electric resistance of the corona plasma is comparable with the electric resistance of the wire core. These observations are in a good agreement with the MHD simulations in this paper that predict almost flat profile for $Q_{\rm Ohm}(r)$. Figure 6(a) presents the radial profiles of the ohmic heating per unit volume of plasma for the simulations with the truncated and full current pulses. In the latter case the extension of the plasma corona in the radial direction is larger than in the former case. In its turn the larger corona extension predetermines the lower level of $Q_{\rm Ohm}$, as the electric current distributes through the larger cross section.

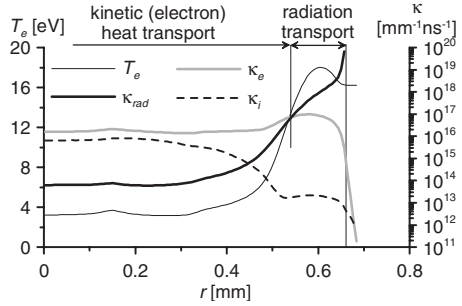

FIG. 5. Radial profiles of the radiation diffusion coefficient $\kappa_{\rm rad}$ and the electron κ_e and ion κ_i heat transport coefficients at maximum current ($t=60$ ns). Radiation heat transport exceeds the kinetic heat transport in the region behind the radiating surface, where $\kappa_{\rm rad} \gg \kappa_e, \kappa_i$.

In both simulations, presented in Fig. 6(a), the radiation power losses due to the limited outward radiation flux $F_{\rm rad}(r_s)=\sigma T_e^4(r_s)$ [Eq. (27)] significantly exceed the local ohmic heating $Q_{\rm Ohm}(r_s)$. By trapping the radiation inside, the opaque plasma acts as a blanket, creating the higher temperature zone inside the opaque plasma region, behind the radiating surface (see temperature profiles in Fig. 2). Heat trans-

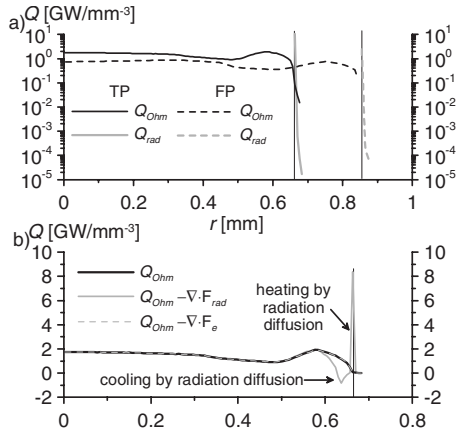

FIG. 6. (a) The intensity of the local ohmic heating $Q_{\rm Ohm}$ and the local radiative cooling $Q_{\rm rad}$ of the unit volume of plasma in simulations with the truncated current pulse (TP) [$t=60$ ns] and the full current pulse (FP) [$t=120$ ns]. (b) Radial profile of $Q_{\rm Ohm}$ and the contributions from the divergence terms for the radiation flux $-\nabla\cdot\mathbf{F}_{\rm rad}$ and electron thermal flux $-\nabla\cdot\mathbf{F}_e$ [Eq. (24)] at maximum current (TP). Fine vertical lines on both plots (a) and (b) mark the positions of the radiating surfaces.

port from these higher temperature zones toward the radiating surface maintains the power balance, compensating for the radiation power losses at $r=r_s$.

In the early simulations of the heterogeneous deuterium Z pinches [21,24] the radiation effects were not strong enough to significantly affect the power balance in plasma. In this case the peak plasma temperature has been reached at the edge of the pinch corona. The same effect is reproduced in the simulation without radiation [Fig. 1(c)], which also predicts much higher peak temperature $T_e=25$ eV (versus the peak $T_e=18$ eV in the truncated current pulse simulations with radiation).

Detailed power balance in the electron component of plasma for the simulation with the truncated current pulse is shown in Fig. 6(b). In the outer corona the heat transport from the zone of maximum temperature toward the radiating surface is provided by the radiation diffusion mechanism, which local efficiency $-\nabla\cdot\mathbf{F}_{\mathrm{rad}}$ at this plasma region is comparable with the local ohmic heating Q_{Ohm}. Plots in Fig. 6(b) show that the radiation heat transport cools down the hottest plasma region and heats up the edge of the opaque plasma region, compensating for the radiation power loss at $r=r_s$.

According to the information presented in Fig. 6, the core and the inner corona regions are heated up exclusively by the ohmic heating, while the contributions due to the convergence of the radiation flux $-\nabla\cdot\mathbf{F}_{\mathrm{rad}}$ and the electron heat flux $-\nabla\cdot\mathbf{F}_e$ are negligible (the same holds for the ion heat flux, as we compare κ_e and κ_i in Fig. 5). This result, however, has only limited applications to the experiments with the exploding metallic wires of the diameter of a few microns, where the thermal flux from the hot corona is believed to be mostly responsible for heating the cooler wire core. There are two fundamental reasons for that.

The intensity of the diffusion effects is inversely proportional to the square of the typical size of plasma spatial inhomogeneities. By switching from the millimeter scale temperature gradients to the micron scale gradients we can significantly increase role of the heat transfer due to the kinetic transport or the radiation diffusion. Also, by decreasing the wire corona radius one can substantially increase the magnetic field intensity, and, as a result, the electron magnetization factor. Thus, the electron heat transport will be further suppressed, as compared to the one shown in Fig. 5, while heat flux due to the radiation diffusion may become the dominant mechanism of the wire core heating. The latter scenario has been reported in the simulations of the steady-state radiation ablation in the wire array Z pinch in Ref. [36].

Another reason is the increasing role of the inductive effects during the fast energy input into the plasma of exploding wire. As it was demonstrated in a number of experimental works (see, for example, Refs. [35,37–39]), the deposition of the electromagnetic field energy into a wire core significantly diminishes after the formation of a highly conductive corona at the wire surface, which works as an inductive barrier for the further energy deposition into a core. In simulations this effect is typically reproduced by the artificial reduction of the electrical conductivity of the core plasma by a factor of 100, which drives the current out of the wire core [36]. Lesser amount of the electric current through the core effectively reduces the intensity of the ohmic heating, and

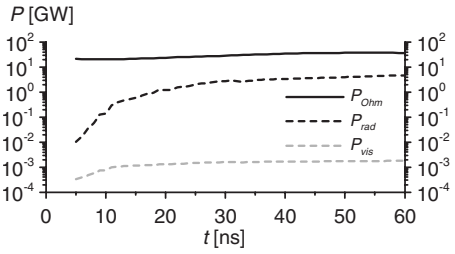

FIG. 7. Evolution of the volume integrated powers of the ohmic heating P_{Ohm}, total radiation P_{rad}, and the visible light emission P_{vis} inside the wavelength range 400–750 nm.

increases the role of the heat flux from the hot corona in heating and ablation of the wire core.

The axial component of the electric field, associated with the inductive effects, can roughly be estimated as $E_z^{(\mathrm{ind})}(r)\sim(\mu_0/2\pi)\ln(r_0/r)dI/dt$, where r_0 is the radius of the return current can. As the liner compression experiments are characterized by lesser derivatives dI/dt and much higher radii r than the ones in the wire array Z-pinch experiments, the inductive effects should be much less significant in the former case. However, the simulation results presented in this paper are still applicable to the wire array Z-pinch experiments at the stage of the current maximum, when $dI/dt\approx 0$.

The evolutions of the volume integrated ohmic heating of plasma P_{Ohm} and radiation power P_{rad} are shown in Fig. 7. At maximum current $P_{\mathrm{Ohm}}=37$ GW, which corresponds the electric field intensity $E_z\approx 2$ kV/mm in a plasma column of $l_z=20$ mm height, or the total voltage drop of 40 kV. Total radiation power at maximum current $P_{\mathrm{rad}}=4.7$ GW corresponds to the radiation from the cylindrical surface of the radius $r_s=0.66$ mm and the temperature $T=16$ eV. Thus, the fraction of the radiation power is only 13% of the total deposited power. This is very different from the case of the imploding wire arrays, where the radiation power fraction exceeds 50% at the implosion stage and is almost 100% at the pinch stagnation stage (see, for example, Ref. [25]).

One can estimate analytically the total deposition of the electromagnetic energy W_{Ohm} per unit length of the load due to the ohmic heating of plasma for the period $[0,t_{\mathrm{sh}}]$, which was excluded from the simulation with the truncated current pulse. Assuming the same load resistance per unit length $R_z=E_z/I_{\max}=2\times 10^{-3}\ \Omega/\mathrm{mm}$, we can calculate W_{Ohm} as

$$W_{\mathrm{Ohm}}=\int_0^{t_{\mathrm{sh}}}E_zIdt=R_z\int_0^{t_{\mathrm{sh}}}I^2dt. \tag{29}$$

Using the current pulse shape $I(t)$, defined by Eq. (4), we get $W_{\mathrm{Ohm}}=7$ J/mm.

As it was discussed in the previous section of this paper, instead of the room temperature 0.026 eV, the higher value of 1 eV was taken as the initial temperature of the load material. In the latter case the excess thermal and ionization energies can be estimated as 11 and 2.6 J/mm, respectively. As we can see, the sum of these two contributing terms is about equal to the energy deposited by the ohmic heating during the first half of the realistic current pulse, given by

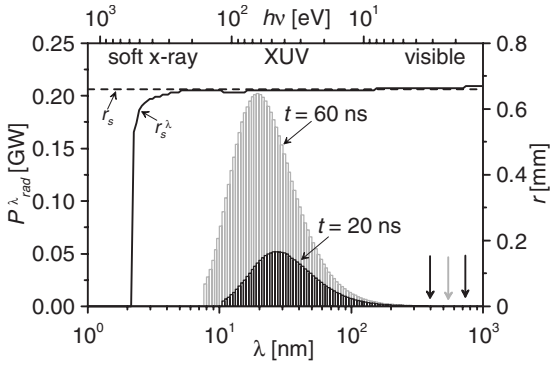

FIG. 8. Spectrally resolved volume integrated radiation power $P^{\lambda}_{\mathrm{rad}}(\lambda,\Delta\lambda)$ at $t=20$ ns and $t=60$ ns. Abscissa axes are shown for both photon wavelength λ and photon energy $h\nu$. Black dotted line shows the boundary $r=r_s$ of the opaque plasma region in one group approximation at $t=60$ ns. Black solid line shows spectrally resolved boundary $r^{\lambda}_s(\lambda)$ of the opaque plasma region. The sensitivity ranges for the streak camera and photodiode detector are shown by the black vertical arrows and by the gray vertical arrow, respectively.

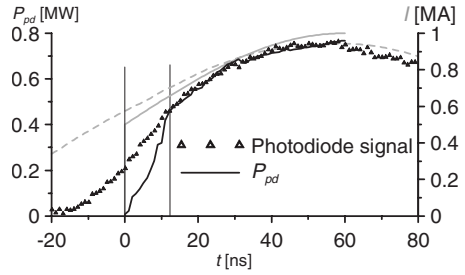

FIG. 9. Qualitative comparison of the measured and calculated intensity of the green light emission from the load plasma. Bold solid line represents the volume integrated radiation power P_{pd} in the wavelength range 495–565 nm, reconstructed from the simulation data. This wavelength range corresponds to the sensitivity range 530 ± 35 nm of the photodiode with the Kodak Wratten No. 58 filter. The experimental photodiode signal is shown in arbitrary units and is represented by the symbols. Fine vertical lines denote the period of the accelerated corona plasma production. Broken gray line represents the experimental current pulse. Solid gray line represents the current pulse, used in simulations [Eq. (5)].

Eq. (4). It should be noted here that according to Eq. (29) W_{Ohm} strongly depends on the parameter t_{sh}. For example, $W_{\mathrm{Ohm}}=13$ J/mm at $t_{\mathrm{sh}}=70$ ns.

The MHD model in the code POS explores the one group radiation model. One of the advantages of this model is the high speed of the computations. However, through the off-line processing we can also perform rough estimation of the dependence of key radiation parameters, such as the emitted radiation power, on the radiation frequency. For example, instead of the integration over the whole spectral range $[0,\infty]$ in Eq. (23), one can narrow down the integration limits and calculate radiation power per unit volume $Q^{\lambda}_{\mathrm{rad}}(\lambda,\Delta\lambda)$ in the wavelength range $[\lambda_n,\lambda_n+\Delta\lambda_n]$.

Volume integrated spectrally resolved radiation power $P^{\lambda}_{\mathrm{rad}}(\lambda,\Delta\lambda)$ is shown versus the wavelength λ at the moments $t=20$ ns and $t=60$ ns in Fig. 8. The radiation power spectrum is similar to the Planckian black-body radiation spectrum. This result is not surprising, provided that the most radiation is coming from the edge of the opaque plasma region, which is a black-body radiator. As the corona plasma heats up, the radiation power increases with the increase of energy of the emitted photons.

As we can see in Fig. 8 most of the radiation power is emitted in the ultraviolet (uv) spectral range, or, to be more exact, near the boundary $\lambda<30$ nm of the extreme uv (xuv) region. The major diagnostic equipment used in the experimental campaign at the Zebra facility was sensitive to the radiation in the visible light range 400–750 nm, which is located at the tail of the Planckian spectral curve. As we can see from Fig. 7, the total radiation intensity in the sensitivity range of the streak camera (shown by black downward arrows in Fig. 8) is only about 1.8 MW at maximum current, which is more than three orders of magnitude less than the total radiation power.

In the same way we can apply the integration in the wavelength range $[\lambda_n,\lambda_n+\Delta\lambda_n]$ to Eq. (22) in order to obtain the spectrally resolved parameter $l^{\lambda}_R(\lambda,r)$. Now we can find the boundary of the opaque plasma regions r^{λ}_s for the different photon energies by solving the implicit equation $l^{\lambda}_R(\lambda,r^{\lambda}_s)=a$.

Spectrally resolved coordinate $r^{\lambda}_s(\lambda)$ of the boundary of the opaque plasma region at maximum current is shown in Fig. 8. For most of the emitted radiation (photon energies $h\nu<200$ eV) spectrally resolved boundary r^{λ}_s almost perfectly coincides with r_s, calculated in one group approximation. As we can see from the data in Fig. 8, the whole plasma region becomes transparent for the high-energy photons $h\nu>600$ eV. However, even such high-energy photons are unlikely to penetrate the core region because of the strong scattering in the high-density core plasma.

C. Comparison with experimental data

The diagnostic equipment in Zebra experiments, based on the radiation features of the corona plasma, did include the photodiode and the optical streak camera. It is quite a complex procedure to properly calibrate the experimental data acquired by these devices in order to extract the exact numbers for plasma parameters. Yet, it is possible to perform the qualitative comparison of raw experimental data with the post-processed simulation results.

The photodiode detects the intensity of the green light photon emission. Separation of the photons of the required energies is performed by using the Kodak Wratten No. 58 filter with the wavelength transmission window 530 ± 35 nm. Assuming an isotropic photon emission from the corona plasma, the photodiode signal should be directly proportional to the volume integrated radiation power P_{pd} in the wavelength range 495–565 nm.

Qualitative comparison of the volume integrated radiation P_{pd} power versus the photodiode signal is given in Fig. 9. In a real experiment the current through plasma gradually rises from 0 to 1 MA in a 120 ns period. However, in the simulation with truncated current pulse the sudden increase of the

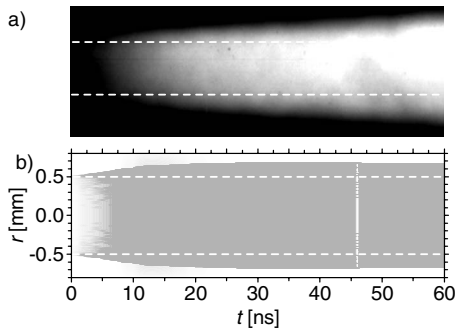

FIG. 10. (a) Streak camera image for Zebra shot No. 892. (b) Integrated surface radiation power from the load (volume radiation power integrated along the line of sight), calculated from the simulation data. Streak camera image is resized and scaled to fit the computation time range 0–60 ns. White dotted lines represent the initial position of the load surface.

electric current to the level of 0.5 MA at the initial moment is assumed. At these conditions we should allow a few nanosecond period for the corona production with the accelerated rate as compared to the experiments. As we can see from Fig. 9 this period of the accelerated corona plasma production lasts approximately 12 ns. After that the volume radiation power P_{pd} reproduces the shape of the photodiode signal with a very good accuracy.

While the photodiode signal provides the data about the volume integrated radiation power, the streak camera provides spatially resolved in one dimension (along the load radius) information about the evolution of the radiation power, assuming the plane projection. These types of data can also be reconstructed by post-processing the radiation dynamics data obtained in simulation. We can calculate the radiation intensity $Q_{\mathrm{vis}}(r,t)$ in the unit volume in the visible light wavelength range 400–750 nm, which corresponds to the sensitivity range of the streak camera. Then, the qualitative comparison with the streak camera image can be performed by assuming the perfect azimuthal symmetry of the plasma configuration and integrating $Q_{\mathrm{vis}}(r,t)$ along the line of sight.

As we can see from the analysis of the data, presented in Fig. 10, the streak camera image mostly represents the expansion dynamics of the radiating surface (compare, for example, Figs. 4 and 10). This result is not surprising since the radiating surface emits the most power. Yet, it should be noted here that the streak camera is able to catch less than 0.1% of the total radiation power at current pulse maximum (compare P_{rad} and P_{vis} in Fig. 7), since the streak camera sensitivity range is far at the tail of the spectral curve, as shown in Fig. 8.

Very often the traditional laser diagnostics of plasma, such as the laser interferometry, is turned to be ineffective for probing the plasma objects, created by 1 MA electric discharge. In many occasions the basic reason is the generation of dense plasma formations, which are impenetrable for laser radiation. Yet, even in that case valuable information can still be provided by laser shadowgraphy.

In order to reconstruct the laser shadowgraphy from the simulation data, one has to calculate the coefficient K_λ of the

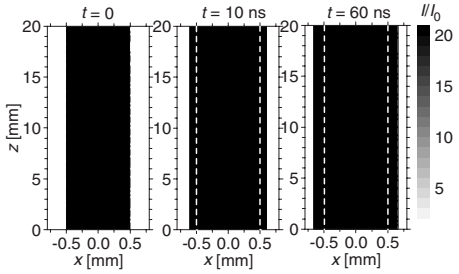

FIG. 11. Contour maps of the intensity of the laser radiation I ($\lambda=528$ nm) that penetrated load plasma normalized by the intensity I_0 of the incident laser radiation (laser shadowgraphy images), reconstructed from the simulation data. Relative intensities $I/I_0 < 20$ are marked by the black color. White dotted lines denote the initial position of the load surface.

extinction of laser radiation with a wavelength λ in plasma. If we take for simplicity $K_\lambda = 1/l_R^\lambda$, then for low energy photons $h\nu \ll \chi_m$

$$K_\lambda = \frac{e^6 T_e \lambda^3}{\varepsilon_0^3 c^4 h^4} \frac{e^{hc/\lambda T_e} - 1}{12\sqrt{3}\pi} \sum_{m=1}^{Z} m^2 N_m e^{-\chi_m/T_e}. \tag{30}$$

Reconstructed laser shadowgraphy data are presented in Fig. 11. As we can see from the data in Fig. 8, the position of the boundary of the plasma region that is opaque to the green laser radiation r_s^λ almost perfectly coincides with the edge of the opaque plasma region r_s in one group approximation. In this sense the shadowgraphy diagnostics observes the same object as the one recorded by the streak camera in Fig. 10(a). However, the laser shadowgraphy images provide spatial resolution in both radial and axial directions. Thus, this diagnostics can be use to trace the instability growth at the outer edge of the corona plasma region.

Because of the steepness of the gradient at the outer edge of the corona the laser shadowgraphy provides no shades of gray, as most of the corona plasma is impenetrable for the green light radiation (see r_s^λ plot in Fig. 8). Yet, by increasing the energy of the probing photons above the keV level we should be able to see the inner corona structure. This diagnostic technics is known as x-ray backlighting, implementing such x-ray sources as, for example, the x pinch [40], or the monochromatic x-ray emission from the laser targets [41]. The latter direction looks the most promising one at the Nevada Terawatt Facility as the short-pulse 100 TW Leopard laser is expected to be online soon.

IV. CONCLUSION

The evolution of plasma formed at the surface of the metallic load can be described by the radiation MHD model in the core-corona approximation, used in MHD simulations of heterogeneous Z pinches. According to the latter approximation the bulk of the load material is associated with the cold pinch core, while the plasma produced at the load surface forms the hot corona.

The radiation MHD simulations show that a relatively small fraction ($\approx 13\%$) of the total deposited power is con-

verted into the radiation. The rest of the power ($\approx 87\%$) is deposited directly into the load material through the ohmic heating. Because of the relatively small fraction of radiation in the total balance of power, the influence of the radiation effects on the dynamics of plasma production is not significant. Yet it is the radiation dynamics that defines the plasma temperature and the heat transport in the outer layers of the corona.

The MHD modeling in this paper considered the radiation dynamics of both optically thin (transparent) and optically thick (opaque) plasma regions in a single simulation. It was found that most of the plasma produced at the load surface is opaque. The edge of the opaque plasma region radiates as a black body in the xuv spectral region with the equilibrium radiation temperature 16 eV, while the radiation emission from the transparent plasma region is negligibly small.

By trapping the radiation inside, the opaque plasma serves as the "blanket" for the internal energy (and temperature) of the electron gas. As a result, the maximum of the electron temperature $T_e = 18$ eV is reached inside the corona region, contrary to the classical case of weakly radiating heterogeneous deuterium Z pinches with the maximum temperature at the outer corona edge. The strong radiation energy flux from this high-temperature zone toward the edge of the opaque plasma region feeds the intense black-body radiation, which power exceeds even the local ohmic heating. The latter process provides the effective conversion of the deposited electromagnetic energy into the xuv radiation through the resistive heating of the hottest part of the corona plasma.

Although the theoretical investigation in this paper was related to the experimental campaign at the 1 MA Zebra facility, the general results about the radiation dynamics and structure of the corona plasma, produced at the outer liner surface, can be applied to liner compression experiments at multi-MA long-pulse current accelerators, such as Shiva Star and Atlas. With some modifications the radiation MHD model, developed for the present investigation, can be useful in solutions of the several key problems of wire array dynamics, such as precursor formation and structure of the highly radiating Z pinch at the stagnation phase.

ACKNOWLEDGMENTS

The authors greatly appreciate the help of S. Fuelling, T. Goodrich, and R. Presura in processing of experimental data. The authors are grateful for numerous productive discussions with W. Atchison, J. Degnan, R. Faehl, A. Velikovich, P. Sasorov, N. Bobrova, S. Bulanov, T. Razinkova, S. Garanin, V. Kantsyrev, A. Safronova, M. Cuneo, B. Jones, and S. Rosenthal. This work was supported by DOE-OFES Grants No. DE-FG02-04ER54752 and No. DE-FG02-06ER54892.

[1] J. Wesson, *Tokomaks*, 3rd ed. (Oxford University Press, Oxford, 2004).
[2] J. Lindl, Phys. Plasmas **2**, 3933 (1995).
[3] R. C. Kirkpatrick, I. R. Lindemuth, and M. S. Ward, Fusion Technol. **27**, 201 (1995).
[4] J. H. Degnan *et al.*, IEEE Trans. Plasma Sci. **29**, 93 (2001).
[5] T. P. Intrator *et al.*, IEEE Trans. Plasma Sci. **32**, 152 (2004).
[6] T. Intrator *et al.*, Phys. Plasmas **11**, 2580 (2004).
[7] S. Zhang *et al.*, IEEE Trans. Plasma Sci. **34**, 223 (2006).
[8] A. Esaulov *et al.*, Phys. Plasmas **11**, 1589 (2004).
[9] V. Makhin *et al.*, Phys. Plasmas **12**, 042312 (2005).
[10] R. E. Siemon *et al.*, Nucl. Fusion **45**, 1148 (2005).
[11] I. R. Lindemuth *et al.*, Phys. Rev. Lett. **75**, 1953 (1995).
[12] S. F. Garanin, IEEE Trans. Plasma Sci. **26**, 1230 (1998).
[13] S. F. Garanin, V. I. Mamyshev, and E. M. Palagina, IEEE Trans. Plasma Sci. **34**, 2268 (2006).
[14] R. E. Reinovsky, W. L. Atchison, J. H. Goforth, I. R. Lindemuth, E. A. Lopez, and S. P. Marsh, IEEE Trans. Plasma Sci. **26**, 1454 (1998).
[15] R. E. Reinovsky, IEEE Trans. Plasma Sci. **28**, 1563 (2000).
[16] R. E. Reinovsky *et al.*, IEEE Trans. Plasma Sci. **30**, 1764 (2002).
[17] T. W. Sanford *et al.*, Phys. Rev. Lett. **77**, 5063 (1996).
[18] R. B. Spielman *et al.*, Phys. Plasmas **5**, 2105 (1998).
[19] P. J. Turchi *et al.*, IEEE Trans. Plasma Sci. **30**, 1777 (2002).
[20] R. J. Faehl *et al.*, IEEE Trans. Plasma Sci. **32**, 1972 (2004).
[21] N. A. Bobrova, T. L. Razinkova, and P. V. Sasorov, Sov. J. Plasma Phys. **18**, 269 (1992).
[22] I. R. Lindemuth, G. H. McCall, and R. A. Nebel, Phys. Rev. Lett. **62**, 264 (1989).
[23] I. R. Lindemuth, Phys. Rev. Lett. **65**, 179 (1990).
[24] N. A. Bobrova, T. L. Razinkova, and P. V. Sasorov, Sov. J. Plasma Phys. **14**, 617 (1988).
[25] A. Esaulov, Phys. Plasmas **13**, 042506 (2006).
[26] A. A. Esaulov and P. V. Sasorov, Plasma Phys. Rep. **23**, 576 (1997).
[27] N. A. Bobrova and P. V. Sasorov, Plasma Phys. Rep. **19**, 406 (1993).
[28] A. Esaulov, P. Sasorov, L. Soto, M. Zambra, and J. Sakai, Plasma Phys. Controlled Fusion **43**, 571 (2001).
[29] N. A. Bobrova, A. Esaulov, J. I. Sakai, P. V. Sasorov, D. J. Spence, A. Butler, S. M. Hooker, and S. V. Bulanov, Phys. Rev. E **65**, 016407 (2001).
[30] Ya. B. Zeldovich and Yu. P. Raizer, *Physics of Shock Waves and High-Temperature Hydrodynamic Phenomena* (Academic Press, New York, 1967).
[31] F. S. Felber and N. Rostoker, Phys. Fluids **24**, 1049 (1981).
[32] S. V. Lebedev *et al.*, Phys. Plasmas **8**, 3734 (2001).
[33] G. C. Pomraning, J. Quant. Spectrosc. Radiat. Transf. **27**, 517 (1982).
[34] C. D. Levermore, J. Quant. Spectrosc. Radiat. Transf. **31**, 149 (1984).
[35] G. S. Sarkisov, K. W. Struve, and D. H. McDaniel, Phys. Plasmas **11**, 4573 (2004).
[36] E. P. Yu, B. V. Oliver, D. B. Sinars, T. A. Mehlhorn, M. E. Cuneo, P. V. Sasorov, M. G. Haines, and S. V. Lebedev, Phys. Plasmas **14**, 022705 (2007).
[37] G. S. Sarkisov, P. V. Sasonov, K. W. Struve, D. H. McDaniel,

P. V. Sasorov, A. N. Gribov, and G. M. Oleinik, Phys. Rev. E **66**, 046413 (2002).
[38] G. S. Sarkisov, P. V. Sasorov, K. W. Struve, and D. H. McDaniel, J. Appl. Phys. **96**, 1674 (2004).
[39] A. G. Rousskikh *et al.*, IEEE Trans. Plasma Sci. **34**, 2232 (2006).
[40] S. V. Lebedev *et al.*, Rev. Sci. Instrum. **72**, 671 (2001).
[41] D. B. Sinars *et al.*, Rev. Sci. Instrum. **75**, 3672 (2004).